

Many-body localized hidden Born machine

Weishun Zhong^{1,2} Xun Gao³ Susanne F. Yelin³ and Khadijeh Najafi⁴

¹*Department of Physics, Massachusetts Institute of Technology, Cambridge, MA, USA*

²*IBM Quantum, MIT-IBM Watson AI Lab, Cambridge MA, 02142, USA*

³*Department of Physics, Harvard University, Cambridge, Massachusetts 02138, USA*

⁴*IBM Quantum, IBM T.J. Watson Research Center, Yorktown Heights, NY 10598 USA*

Born Machines are quantum-inspired generative models that leverage the probabilistic nature of quantum states. Here, we present a new architecture called many-body localized (MBL) hidden Born machine that uses both MBL dynamics and hidden units as learning resources. We theoretically prove that MBL Born machines possess more expressive power than classical models, and the introduction of hidden units boosts its learning power. We numerically demonstrate that the MBL hidden Born machine is capable of learning a toy version of MNIST handwritten digits, quantum data obtained from quantum many-body states, and non-local parity data. In order to understand the mechanism behind learning, we track physical quantities such as von Neumann entanglement entropy and Hamming distance during learning, and compare the learning outcomes in the MBL, thermal, and Anderson localized phases. We show that the superior learning power of the MBL phase relies importantly on both localization and interaction. Our architecture and algorithm provide novel strategies of utilizing quantum many-body systems as learning resources, and reveal a powerful connection between disorder, interaction, and learning in quantum many-body systems.

I. INTRODUCTION

The computational power of quantum processors is the subject of considerable amount of recent research, in particular with regard to scaling and a potential quantum advantage^{1–7}. While the advent of a fully error corrected quantum computer requires yet another milestone, the immediate application of noisy quantum hardware with a clear advantage over classical computation becomes even more crucial. In this regard, the interface of quantum computing and machine learning has been increasingly brought into focus. For example, the rise of hybrid variational algorithms such as variational quantum eigensolvers (VQE)⁸ and the quantum approximate optimization algorithm (QAOA)⁹, utilizing a parametrized quantum circuit as variational ansätze and optimizing the parameters classically has been considered as particularly promising as they aim to obtain heuristic and approximate solutions.

However, the exponential dimension of the Hilbert space and the random characteristics of parametrized quantum circuits makes their training very challenging due to the existence of barren plateaus¹⁰. More recently, yet another approach to quantum machine learning has emerged, which is known as brain-inspired^{11–15}. One interesting category consists of quantum reservoir computing (QRC) where a fixed reservoir geometry scrutinizing the unitary dynamics of an interacting quantum system allows versatile machine learning tasks^{16–19}. While QRCs have shown many advantages, they are mainly appropriate for discriminative tasks such as classification or regression.

The goal of generative models, however, is to learn an unknown data probability distribution p_{data} in order to subsequently sample from p_{data} and thus generate new and previously unseen data. Such tasks can, for example, be performed by the recently introduced Born

machines^{20,21}. Born machines for many-body problems have early on shown to be successful in conjunction with tensor network state ansätze. The elements of these matrix product states or tree tensor networks and their bond dimensions can be optimized during training to effectively approximate p_{data} ^{20–22}. While Born machines have also been tested with parameterized quantum circuits²³, we address here the question of whether there are other quantum many-body states that can be used as ansatz for Born machine to any advantage.

Quantum many-body systems display many phases in the presence of disorder, in particular, the break-down of thermalization and thus localization of the wavefunction in the so-called *many-body localized* (MBL) phase. Here, emergent integrals of motion can be utilized as quantum memories²⁴. The failure of such systems to anneal²⁵ has inspired their use in QRC¹⁹ for learning tasks, with particular enhancement close to the phase transition²⁶.

Here, we extend quantum inspired generative models into the MBL phase, and introduce a hidden architecture to increase the representation power of our generative model. While recent work has also studied Born machines in the MBL phase²⁷, using a similar quenched approach, our work differs in the hidden architecture and the characterization of learnability and expressibility.

In this article, we first introduce the hidden Born machine in section II, and prove that including hidden units into Born machine leads to expressive power advantage with respect to the basic architecture. Then, in section III, we comment on the expressibility of the MBL-Born machine, leveraging the fact that our model can be mapped into existing models with proven advantage in expressibility over classical models²⁸. We describe our training algorithm in section IV and introduce the randomly driven Born machine in section IV B and compare its performance with the hidden Born machine by learning patterns of MNIST hand written digits. Next, in sec-

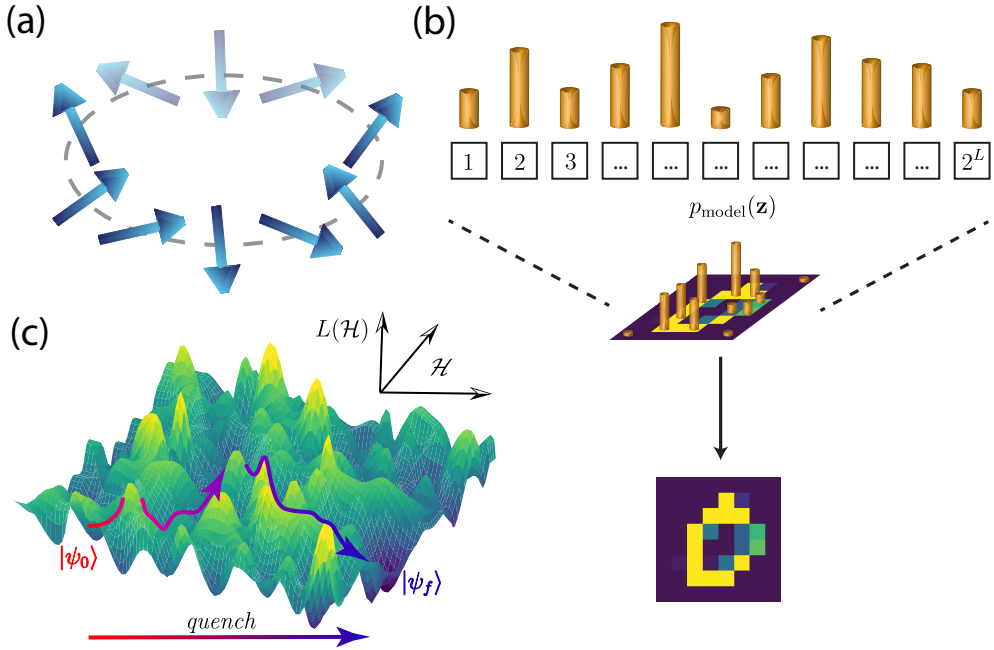


Figure 1: Illustration of the MBL hidden Born machine. (a) XXZ spin chain in 1D with periodic boundary condition. The faded color spins are the hidden units h_i , and the solid color spins are the visible units v_i . (b) The probability distribution of finding individual states in the z-basis represents the model distribution for the generative model, which are coded as normalized pixel values of an image. (c) An illustration of the loss landscape defined by our hidden MBL Born machine. The training is done by optimizing disorder configurations in the Hamiltonian during each quantum quench, which is then used to evolve the initial state $|\psi_0\rangle$ over successive layers of quenches toward a final state $|\psi_f\rangle$ which gives rise to the desired model distribution.

tion V we investigate the learning power of the hidden Born machine both in the thermal phase and the MBL phase, and numerically show that the thermal phase fails to learn data obtained from quantum systems either in MBL or in thermal phase. Tracking von Neumann entanglement entropy and Hamming distance during training suggests that localization is crucial to learning. In section V C we further show that while the hidden Born machine trained in the MBL phase is able to capture the underlying structure of the parity data, a hidden Born machine trained in the Anderson localized phase fails to do so, shedding light on the fact that the interplay between interaction and disorder plays an important role in learning. Finally, we conclude and discuss possible direction for future works.

II. HIDDEN BORN MACHINES

Born machine^{29–33} is a generative model that parameterized the probability distribution of observing a given configuration \mathbf{z} of the system according to the probabilistic interpretation of its associated quantum wavefunction $\psi(\mathbf{z})$,

$$p_{\text{Born}}(\mathbf{z}) = \frac{|\psi(\mathbf{z})|^2}{\mathcal{N}}, \quad (1)$$

where $\mathcal{N} = \sum_{\mathbf{z}} |\psi(\mathbf{z})|^2$ is the overall normalization of the wavefunction. Note that \mathcal{N} is only required in tensor network ansätze but not in physical systems. Training of the Born machine is done by minimizing the discrepancy between the model distribution $p_{\text{Born}}(\mathbf{z})$ and the data distribution $q_{\text{data}}(\mathbf{z})$.

In the language of Boltzmann machine^{34–36}, the units that are used for generating configurations are called ‘visible’. Meanwhile, adding ‘hidden’ units prove to be a powerful architecture for the Boltzmann machine as it provides a way to decouple the complex interaction among the visible units at the expense of introducing interaction between the hidden and the visible units^{37,38}. In Eqn.(1), all units of the system are used to generate configurations that are compared against data and therefore all units are visible. In a similar spirit, we introduce hidden units to the Born machine by defining the probability distribution of observing a given visible spin configuration \mathbf{z} to be its expectation value in z -basis after tracing out the hidden units,

$$p_{\text{hidden}}(\mathbf{z}) = \text{Tr} \rho_{\text{vis}} \Pi_Z, \quad (2)$$

where

$$\rho_{\text{vis}} = \text{Tr}_h |\psi\rangle\langle\psi|, \quad (3)$$

is the reduced density matrix for the visible units, and $\Pi_Z = |\mathbf{z}\rangle\langle\mathbf{z}|$ is the projection operator onto the z -basis

of the visible part of the system (see Fig.1(a) for an illustration of our model). Note that normalization is implicit in Eqn.(3) for ρ_{vis} to be a density matrix.

We argue that the hidden Born machine in Eqn.(2) offers expressive power advantage over the basic Born machine in Eqn.(1). We demonstrate this by first proving a proposition about the hidden architecture, showing that adding hidden units generalizes the basic Born machine and therefore the achievable generalization error is at least as good as the original one. While our proof is independent of the particular choice of Hamiltonian, we support our claim with numerical evidence of a hidden Born machine realized with a XXZ spin chain in section IV.

A. The hidden advantage

In this section, we prove that the hidden Born machine Eqn.(2) generalizes the basic Born machine (BM) defined by Eqn.(1), in the sense that the class of probability distributions expressible by the basic Born machine is a subset of that of the hidden Born machine. In the following, we assume only that the visible and hidden part couple through an interaction term in the Hamiltonian.

Let's consider a basic Born machine consisting of only visible units $\mathbf{v} = \{v_i\}$, with Hamiltonian $\hat{\mathcal{H}}_v$. Now consider adding hidden units $\mathbf{h} = \{h_j\}$ to the system with Hamiltonian $\hat{\mathcal{H}}_h$ and the hidden units couple with the visible ones through an interaction Hamiltonian $\hat{\mathcal{H}}_{\text{int}}$. The full Hamiltonian can be written as

$$\hat{\mathcal{H}}_{vh}[\mathbf{v}, \mathbf{h}] = \hat{\mathcal{H}}_v[\mathbf{v}] + \hat{\mathcal{H}}_h[\mathbf{h}] + \hat{\mathcal{H}}_{\text{int}}[\mathbf{v}, \mathbf{h}], \quad (4)$$

where all the $\hat{\mathcal{H}}$'s in general can be time-dependent. Let's assume that the basic Born machine model is described by just the visible part of Hamiltonian in Eqn.(4), $\hat{\mathcal{H}}_{\text{BM}} = \hat{\mathcal{H}}_v(\Theta^{\text{BM}})$, and the hidden Born machine is described by the full Hamiltonian, $\hat{\mathcal{H}}_{\text{hBM}} = \hat{\mathcal{H}}_{vh}(\Theta^{\text{hBM}})$, where Θ^{BM} and Θ^{hBM} denotes the parameters in the Hamiltonian to be optimized during learning.

Proposition 1. *For the same set of visible spins \mathbf{v} , let $p_{\text{BM}}(\mathbf{z})$ denote the model distribution realized by the basic Born machine, and $p_{\text{hBM}}(\mathbf{z})$ denote the model distribution realized by the hidden Born machine, then $\{p_{\text{BM}}(\mathbf{z})\} \subseteq \{p_{\text{hBM}}(\mathbf{z})\}$.*

Proof. Let's denote the initial state for the BM as $|\psi_0^v\rangle \in \mathcal{H}_v$. Let $\hat{\mathcal{U}}_v = \hat{\mathcal{T}} \exp\left(-i \int_0^T dt \hat{\mathcal{H}}_v\right)$. Then, the final state of BM is $|\psi_f^v\rangle = \hat{\mathcal{U}}_v |\psi_0^v\rangle$. Choose an initial product state for the hBM, $|\psi_0^{vh}\rangle = |\psi_0^v\rangle \otimes |\psi_0^h\rangle \in \mathcal{H}_v \otimes \mathcal{H}_h$ for some $|\psi_0^h\rangle \in \mathcal{H}_h$. Choose Θ^{hBM} to be such that $\hat{\mathcal{H}}_v^{\text{hBM}} = \hat{\mathcal{H}}_v^{\text{BM}}$, and $\|\hat{\mathcal{H}}_v^{\text{hBM}}\| \gg \|\hat{\mathcal{H}}_{\text{int}}^{\text{hBM}}\|$.

Then, we have

$$|\psi_f^{vh}\rangle \approx \hat{\mathcal{U}}_v |\psi_0^v\rangle \otimes \hat{\mathcal{U}}_h |\psi_0^h\rangle = |\psi_f^v\rangle \otimes |\psi_f^h\rangle \quad (5)$$

where we have defined $|\psi_f^h\rangle \equiv \hat{\mathcal{U}}_h |\psi_0^h\rangle$. With this choice, now $\rho_{\text{vis}} = \text{Tr}_h |\psi_f^{vh}\rangle \langle \psi_f^{vh}| = |\psi_f^v\rangle \langle \psi_f^v|$, and $p_{\text{hBM}}(\mathbf{z}) = \text{Tr} \rho_{\text{vis}} \Pi_Z = |\psi_f^v(\mathbf{z})|^2 = p_{\text{BM}}(\mathbf{z})$, where p_{BM} is automatically normalized ($\mathcal{N} = 1$) for physical systems as in our case. Therefore, the class of probability distributions described by BM is contained in hBM. \square

Corollary 2. *Comparing the achievable loss \mathcal{L} of the hidden Born machine and the basic Born machine on any given loss function, we have $\mathcal{L}_{\text{hBM}} \leq \mathcal{L}_{\text{BM}}$.*

Prop.1 suggests that the hidden Born machine is able to represent a larger class of probability distributions and thus generalizes the basic Born machine. Cor.2 indicates that the achievable training loss for the hidden Born machine is less than or equal to that of the regular Born machine, a property that we will confirm numerically in section IV.

III. EXPRESSIBILITY OF MBL-BORN MACHINE

Previously, different ansätze for $|\psi\rangle$ has been introduced for the Born machine, notably tensor networks states and states prepared by both digital quantum circuits and analog quantum many-body systems^{20,21,23,27}. In this paper, we will be adopting the latter approach, and focus on a specific type of quantum many-body systems that admits a many-body localization (MBL) phase. In the following, we first discuss the simple model that give rise to the MBL phase. Then, leveraging on the fact that the XXZ model under appropriate choice of quench parameters can be mapped into a 2D Ising model that has quantum computational advantage²⁸, we show that our MBL Born machine possesses more expressive power than classical models.

A. Many-body localized ansätze

It is generally believed that, thermalization in quantum system wipes out the microscopic information associated with the initial state. Even in the case of closed quantum system, the information of initial state quickly spreads throughout the entire system, implying that no local measurements can retrieve those information^{39,40}. However, it's known that strong disorder leads to localization, preventing the system to thermalize. Furthermore, the localization manifests itself in the form of memory associated with the lack of transport. While the localization in the presence of strong disorder was first introduced in non-interacting systems by Anderson⁴¹, more recently, it was shown that the localization and break down of thermalization can also happen in strongly interacting systems, leading to new dynamical phase of matter known as many-body localization (MBL)^{42,43}.

In the MBL phase, eigenstates of the system do not satisfy Eigenstate Thermalization Hypothesis (ETH) and the wavefunctions become localized in the Hilbert space. Such ergodicity breaking renders the system to retain memory of its initial state, and offers advantage in controlling and preparing desired quantum many-body states and has been also realized experimentally⁴⁴. The XXZ model of quantum spin chain is well-known to develop a MBL phase when the disorder strength exceeds the MBL mobility edge⁴⁵.

We perform numerical simulation with the XXZ-Hamiltonian $\hat{\mathcal{H}}_{\text{XXZ}}$ defined as:

$$\hat{\mathcal{H}}_{\text{XXZ}} = \sum_i^{L-1} J_{xy} (\hat{S}_i^x \hat{S}_{i+1}^x + \hat{S}_i^y \hat{S}_{i+1}^y) + \sum_i^{L-1} J_{zz} \hat{S}_i^z \hat{S}_{i+1}^z, \quad (6)$$

where $\hat{S}_i^\alpha (\alpha \in \{x, y, z\})$ are Pauli spin 1/2 operators acting on spins $i \in 1, \dots, L$, and $L = L_v + L_h$ consists of L_v visible units and L_h hidden units. J_{xy} and J_{zz} are couplings in the xy plane and z direction, respectively. Then, we consider a series of M quenches $\hat{\mathcal{H}}_{\text{quench}}(\Theta_m)$ in the z -direction:

$$\hat{\mathcal{H}}_{\text{total}} = \hat{\mathcal{H}}_{\text{XXZ}} + \hat{\mathcal{H}}_{\text{quench}}(\Theta_m), \quad (7)$$

where $\hat{\mathcal{H}}_{\text{quench}}(\Theta_m) = \sum_i h_i^m \hat{S}_i^z$ and we have denoted the tunable parameters in the system collectively as $\Theta_m = \{h_i^m\}$. During each quench m , h_i^m are drawn i.i.d. from the uniform distribution over the interval $[-h_d, h_d]$, where h_d is the disorder strength. Notice that when $J_{zz} = 0$, the model reduces to non-interacting XY model with random transverse field exhibiting single particle localization. Once we turn on the J_{zz} interaction, the spins couple via Heisenberg interaction and MBL phase emerges when $h_c \sim 3.5$ (for $J_{zz} = J_{xy} = 1$)⁴⁵⁻⁴⁷. See more details in Appendix A.

In section IV, we will explain the training algorithm under the time evolution implied by series of quenches in $\hat{\mathcal{H}}_{\text{total}}$, and learning through optimizing the values of disordered field h_i^m at each site.

B. Mapping XXZ chain into Ising model

There has been extensive studies on the expressive power of quantum models. In particular, quantum computational advantage for sampling problem has been proved (based on standard computational complexity assumptions) in a translation-invariant Ising model²⁸. While our numeric are mostly restricted to the 1-dimension case as it can be studied by exact diagonalization, the XXZ model can be realized in any dimensions.

In this section, we show that the XXZ model in 2-dimension, with proper choice of disorder parameters, can be reduced to the Ising model in Ref.²⁸, and therefore its expressive power has advantage over classical models.

Proposition 3. *The XXZ model in 2D subject to quench in z -direction can be reduced to an Ising model.*

Proof. In 2D,

$$\hat{\mathcal{H}}_{\text{XXZ}} = \sum_{\langle i,j \rangle} J_{xy} (\hat{S}_i^x \hat{S}_j^x + \hat{S}_i^y \hat{S}_j^y) + \sum_{\langle i,j \rangle} J_{zz} \hat{S}_i^z \hat{S}_j^z, \quad (8)$$

where the interactions are between nearest neighbours. During a quench $\hat{\mathcal{H}}_{\text{quench}}$ of duration t_m , we can separate the disorder into a time-dependent and a time-independent part,

$$h_i^m(t) = J_i^m(t) + B_i^m. \quad (9)$$

In the case that the lattice is a bipartite graph, we can partition the vertices into two partitions, and denote the sites in one partition as $\mathcal{K} = \{k_1, k_2, \dots, k_{L/2}\}$ and another partition as $\mathcal{N} = \{n_1, n_2, \dots, n_{N/2}\}$ (assuming N even). For example, in the case of a square lattice, \mathcal{K} and \mathcal{N} correspond to the black and white sites of the checkerboard coloring. For the set of \mathcal{K} spins, we turn on a π -pulse in the middle of the quench ($k \in \mathcal{K}$), such that:

$$J_k^m(t) = \begin{cases} 0 & \text{if } 0 \leq t < \frac{t_m}{2} \\ \frac{\pi}{2\Delta t} & \text{if } \frac{t_m}{2} \leq t < \frac{t_m}{2} + \Delta t \\ 0 & \text{if } \frac{t_m}{2} + \Delta t \leq t < t_m \end{cases} \quad (10)$$

where $\Delta t \ll t_m$ is a short duration of time. With this choice of disorder, the time evolution operator reduces to

$$\hat{U} = e^{-i\hat{\mathcal{H}}_{\text{XXZ}}\Delta t} (\prod_k i \hat{Z}_k) e^{-i \sum_k B_k^m \hat{Z}_k}. \quad (11)$$

Now the Pauli Z 's effectively flip the signs of the $\hat{X}\hat{X}$ and $\hat{Y}\hat{Y}$ terms in the XXZ-Hamiltonian, and upon integrating over the duration of a quench cancels out with the corresponding terms in first half of the quench. Therefore, after time evolution of a quench, the effective Hamiltonian is left with only Ising interactions,

$$\bar{\mathcal{H}}_{\text{eff}}^m = \sum_{\langle i,j \rangle} J_{zz} \hat{S}_i^z \hat{S}_j^z + \sum_i B_i^m \hat{S}_i^z \quad (12)$$

□

As a result, we have recovered the case in Ref.²⁸ and showed that XXZ model's expressibility has quantum computational advantage⁸⁰.

IV. TRAINING OF HIDDEN MBL BORN MACHINE

A. Learning algorithm

The basic idea behind the training of Hidden Born machine is the following: given target distribution q_{data} , and a loss function $\mathcal{L}(p_{\text{model}}, q_{\text{data}})$ that measures the

discrepancy between model distribution and data distribution, training of the MBL Born machine is achieved through time-evolving the system with the Hamiltonian in Eqn.(6), then optimizing Θ_m over N different disorder realizations for each quench m . After obtaining the final state at the M -th quench, we evaluate the model distribution of the MBL hidden Born machine from Eqn.(2) and use it as our generative model (see Fig.1(c) for an illustration of the learning process). We use Maximum Mean Discrepancy (MMD) loss as our loss function:

$$\mathcal{L}_{MMD} = \left\| \sum_x p(x)\phi(x) - \sum_x q(x)\phi(x) \right\|^2, \quad (13)$$

where $\phi(x)$ are kernel functions that one can choose (see more details in Appendix B).

The learning algorithm is summarized by the pseudo-code in Alg.1.

Algorithm 1 Training of MBL hidden Born machine

```

Initialize the system in some initial state  $|\psi(\Theta_{m=0})\rangle \equiv |\psi_0\rangle$  and choose  $\Theta_0 = \mathbf{0}$ ;
while  $m < M$  do
  while  $n < N$  do
    Sample  $\Theta_m^{(n)}$  uniformly from the interval  $[-h_d, h_d]$ ;
    Time-evolve the state  $|\psi_{m+1}^{(n)}\rangle = \hat{\mathcal{U}}(\Theta_m^{(n)})|\psi_m\rangle$  with
       $\hat{\mathcal{U}} = \hat{\mathcal{T}} \exp \left( -i \int_0^T dt \hat{\mathcal{H}}_{\text{total}} \right)$ ;
    Trace out the hidden units
       $\rho_{m+1}^{(n)} = \text{Tr}_h |\psi_{m+1}^{(n)}\rangle \langle \psi_{m+1}^{(n)}|$ ;
    Compute  $\mathcal{L}(\Theta_m^{(n)})$  from
       $p_{\text{hidden}}^{(n)}(\mathbf{z}) = \text{Tr} \rho_{m+1}^{(n)} \Pi_Z$ ;
     $n \leftarrow n + 1$ 
  end while
   $\Theta_m = \text{argmax}_{\Theta_m^{(n)}} \mathcal{L}(\Theta_m^{(n)})$ ;
   $|\psi_{m+1}\rangle = \hat{\mathcal{U}}(\Theta_m)|\psi_m\rangle$ 
   $m \leftarrow m + 1$ 
end while
Denote the training outcome as  $p_{\text{model}}(\mathbf{z}) = \text{Tr} \rho_M \Pi_Z$ .

```

Given the reduced density matrix ρ_M of the L_v visible spins at the final layer of the quench $m = M$, we compute the model distribution from Eqn.(2), which gives the probability $p_{\text{model}}(\mathbf{z})$ of finding each of the 2^{L_v} basis states \mathbf{z} in the visible part of the system. For learning image data, we then interpret the probabilities as pixel values (normalized to be within 0 and 1), and reshape it into an image of size $2^{L_v/2} \times 2^{L_v/2}$ (see Fig.1(b)). For quantum data, we interpret these probabilities as measurement outcomes obtained from the quantum state. For more details, see Appendix C.

B. Randomly driven MBL Born machine

In classical machine learning, stochasticity is found to have the effect of smoothing out loss landscape and helps

to avoid local minima^{37,48,49}. When introducing the hidden Born machine in Eqn.(2), the hidden units are traced out and effectively act as a heat bath for the remaining visible units and provide a source for stochasticity. In order to understand the extent to which stochasticity aids learning in the hidden Born machine, in this section, we construct a Born machine with random drive that mimics the heat bath. In Fig.3, we numerically demonstrate that the randomly driven Born machine (RDBM) outperforms the basic Born machine, defined in Eqn.(1) without random drives, and approaches the performance of (yet still underperforms) the hidden Born machine trained with Alg.1.

Let's consider the Hamiltonian Eqn.(6) with applied external random drives $\hat{\mathcal{H}}_{\text{RD}}$ in the x -direction (we can also apply random drives in the xy -plane and the result will be similar),

$$\hat{\mathcal{H}}_{\text{RD}}(t) = \sum_i d_i^m(t) \hat{S}_i^x. \quad (14)$$

To model the heat bath, we would like $\{d_i^m(t)\}$ to be like a white noise,

$$\langle d_i^m(t) d_i^m(0) \rangle = 2D\delta(t), \quad (15)$$

where D is the amplitude of the white noise and is proportional to the temperature of the bath. In the simulation, we split the driven interval T into intervals of auto-correlation time τ , and require that Eqn.(15) holds for $t > \tau$. Outside of this correlation time, $d_i^m(t)$ is drawn i.i.d. from $\mathcal{N}(0, \sqrt{2D})$.

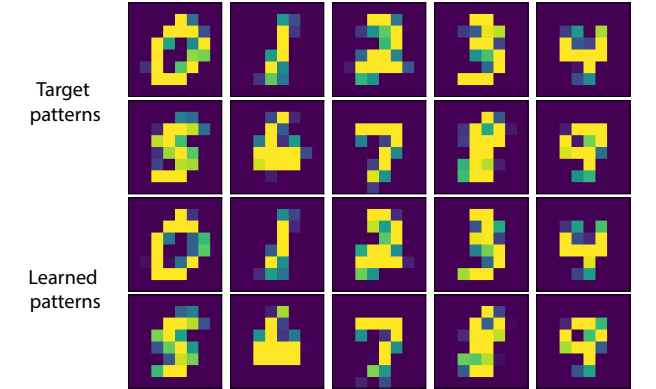


Figure 2: Learning toy MNIST digit patterns. The top two rows are different data instances q_{data} in our toy MNIST digit patterns dataset. The bottom two rows are the corresponding learning outcome p_{model} from our MBL hidden Born machine (each digit trained separately).

To illuminate on the learning power of the hidden Born machine, here, we compare the three models: the basic Born machine, the Randomly Driven Born machine, and the hidden Born machine. We task all three models with a toy dataset constructed from the images of MNIST dataset⁵⁰ (downsampled to 2^{L_v} pixels). Our toy dataset

consists of mean pixel values across all different styles within a single type of MNIST digit, see ‘target patterns’ in Fig.2 (also see Appendix C).

We perform the training of the hidden Born machine using the algorithm described in Alg.1, and show the corresponding learning outcomes in Fig.2. Our results indicate our hidden model is able to learn different patterns of MNIST digits accurately (the result of basic BM and RDBM are omitted).

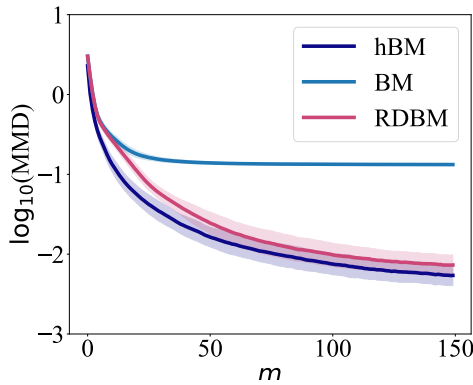


Figure 3: Model comparisons. (a) Basic Born machine(BM), Randomly Driven Born machine(RDBM), and hidden Born machine(hBM). Log-MMD loss as a function of quench layer number m . The solid curves are averaged over 100 different realizations, with one standard deviation included as the shades. The hidden Born machine achieves the lowest MMD loss throughout and at the end of the training.

We plot the loss as a function of quenches m in Fig.3, and we can see that the hidden model performs best out of the three both in terms of final MMD loss on the dataset, with the hierarchy being $\text{hBM} \succeq \text{RDBM} \succeq \text{BM}$.

V. LEARNABILITY IN DIFFERENT PHASES

We have already seen that the hidden Born machine in the MBL phase can properly learn the toy MNIST dataset (Fig.2). An important question arises that whether learning can happen in the thermal phase. In the thermal phase, information spreads throughout the system, which makes it difficult to extract. In the quenched approach as in Eqn.(7), the state of the system in the thermal phase changes wildly between successive quenches and effectively only parameters in the last layer of the quench would be trained. In contrast, as the system becomes more disordered and enters the MBL phase, the breakdown of thermalization and emergence of local integrals of motion leads to local memory, which is useful for directing the state toward a target corner of the Hilber space (Fig.1(c)). We aim to understand the effect of disorder in learning by comparing the learning ability of the hidden Born machine in the MBL and thermal

phases.

In Fig.4(a), we show a log-log plot of the final quench layer MMD loss on the toy MNIST dataset as a function of disorder strength h_d . By varying the disorder strength, the system in Eqn.(6) can exhibit both a thermal phase (denoted as ETH) and an MBL phase depending on whether the disorder strength exceeds the critical value $h_c \sim 3.5$ (for $J_{zz} = J_{xy} = 1$). We observe that the loss value has a significant change at the transition from the thermal phase (corresponding to $h_d < 3.5$ indicated by pink shade) into the MBL phase (indicated by blue shade). The relatively high value of MMD loss in the thermal phase indicates that the hidden Born machine fails to learn. As we increase the disorder, the MMD loss deep in the MBL phase decreases significantly, indicating better learning power of the MBL phase. We can attribute the better learning power in the MBL phase to the quantum memory and the emergent local integral of motions. In contrast to the thermal phase, the thermalization mechanism wipes out all the information from the initial conditions, as observed similarly in the case of quantum reservoir computing in the MBL phase¹⁹.

To better quantify the learning mechanism in the MBL phase, we investigate the time evolution of quantities underlying MBL physics during the quenched steps. First, we investigate the Hamming distance (HD) defined as

$$\mathcal{D}(t) = \frac{1}{2} - \frac{1}{2L} \sum_i \langle \psi_0 | \sigma_i^z(t) \sigma_i^z(0) | \psi_0 \rangle, \quad (16)$$

which gives a measure of number of spin flips with respect to the initial state ψ_0 normalized by the length of chain L . It's expected that in the long time the HD approaches 0.5 in the thermal phase and decreases as one increases the disorder⁵¹. In Fig.4(b), we show the trajectory of HD at the end of each quench $\mathcal{D}^m(t = T)$. We observe that, evolving in the thermal phase the HD fluctuates around the value of 0.5 as expected, while in the MBL phase the HD reaches a lower value about 0.33. The more significant fluctuations in the thermal phase indicate that the system retains little information about the most recent quench, and therefore is difficult to be manipulated toward a target state that gives desired probability distribution. In contrast, the relatively small fluctuations in the MBL phase suggest that system changes gradually between successive quenches and is more amenable to directed evolution by quenches.

One hallmark of MBL phase is the logarithmically slow growth of von Neumann entanglement entropy ($S_{\text{ent}}^m = -\text{Tr} \rho_m \ln \rho_m$) due to the presence of strong interaction. Notice that ρ_m is the reduced density matrix at quench m , which can be obtained by tracing over the complementary part of system with respect to the subsystem of interest. This can be considered as slow dephasing mechanism implying that not all information of initial state survives⁵²⁻⁵⁴. In order to confirm that our system indeed evolves under MBL/thermal dynamics when trained in these two phases, in Fig.4(c), we track the value of S_{ent}^m over different quenches. In the MBL phase, S_{ent}^m shows

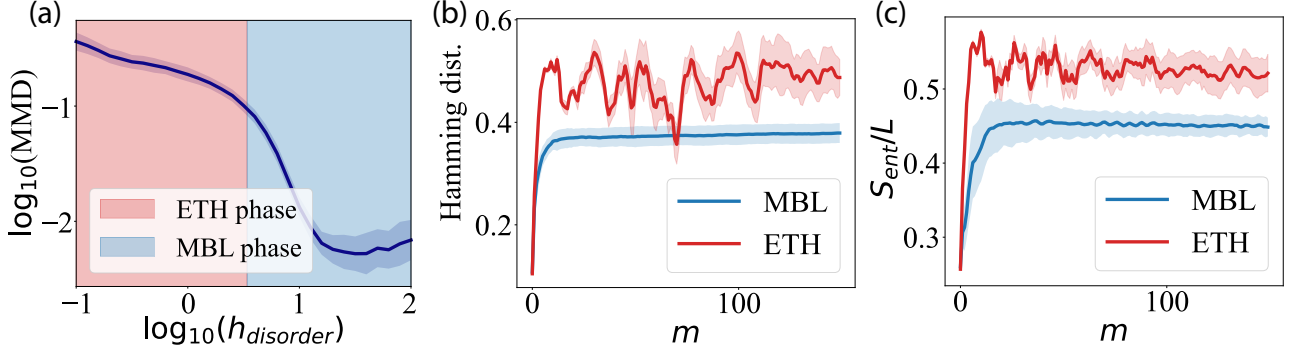


Figure 4: Training hidden Born machine in thermal and MBL phases. (a) The terminal (at the final layer of quench) MMD loss of hidden Born machine on the toy MNIST task is plotted as a function of disorder strength h_d . The results are averaged over 100 realizations and one standard deviation is included as shade. (b) Hamming distance with respect to the initial state (normalized by L) as a function of quenches m . In the thermal phase, states change discontinuously over successive quenches, whereas in the MBL phase states change gradually toward the target state that gives rise to the desired distribution. (c) Entanglement entropy per site as a function of quenches m , confirming that our system evolves under dynamics distinctive in the thermal/MBL phases.

a quick saturation, while in the thermal phase the entanglement entropy changes significantly from successive quenched steps, a behavior expected from the thermal phase.

A. Pattern recognition

Pattern recognition has been implemented in a variety of analog classical systems ranging from molecular self-assembly to elastic networks^{55–62}. It is interesting to ask whether quantum systems possess similar power. In this section, we demonstrate the pattern recognition ability of the MBL hidden Born machine. Here, we take the same toy dataset of MNIST digit patterns as in Fig.2. Each pattern $\xi^\mu \in [0, 1]^{2^{L_v}}$ is a (normalized) vector in the pixel space, where L_v is the length of the visible units, and $\mu = 1, 2, \dots, P$ denotes the pattern index. We encode the patterns into the hidden Born machine by setting $p_{\text{data}} = \sum_\mu \xi^{\mu 81}$. Again, we perform the training of the hidden Born machine using the algorithm in Alg.1 (see first column of Fig.5 for the learned patterns from p_{model}). After training, we obtain the target final state $|\psi_M\rangle$, along with a series of unitaries $\{\hat{\mathcal{U}}(\Theta_m) \equiv \hat{\mathcal{U}}_m\}_{m=0}^M$ that defines the entire history of intermediate states during successive quenches, $|\psi_m\rangle = \prod_{i=0}^m \hat{\mathcal{U}}_{m-i} |\psi_0\rangle$, which upon tracing out hidden units becomes intermediate model distributions, $p_m = \text{Tr} \text{Tr}_h |\psi_m\rangle \langle \psi_m| \Pi_Z$. Now given a partially corrupted pattern $\tilde{\xi}^\mu$ and the state $|\tilde{\psi}^\mu\rangle$ that gives rise to this corrupted pattern, $|\tilde{\psi}^\mu(z)|^2/N = \tilde{\xi}^\mu$ (see second column of Fig.5 for examples of corrupted patterns), we can identify the ‘closest’ intermediate state $|\psi_{m^*}\rangle$ where $m^* = \text{argmax}_m \text{MMD}(\tilde{\xi}^\mu, p_m)$. Then we apply unitary time-evolution to the corrupted state $|\tilde{\psi}^\mu\rangle$ using the series of learned unitaries starting from m^* and ob-

tain the ‘retrieved’ state $|\hat{\psi}^\mu\rangle \equiv \prod_{i=0}^{M-m^*} \hat{\mathcal{U}}_{M-i} |\tilde{\psi}^\mu\rangle$. We can then compute the corresponding retrieved pattern as $\hat{\xi}^\mu \equiv \text{Tr} \text{Tr}_h |\hat{\psi}^\mu\rangle \langle \hat{\psi}^\mu| \Pi_z$ (see last column of Fig.5 for the retrieved patterns).

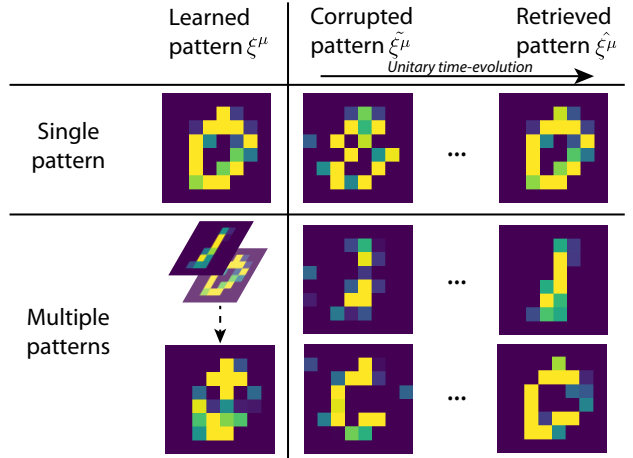


Figure 5: Pattern recognition task by the MBL hidden Born machine. Given a corrupted pattern $\tilde{\xi}^\mu$ and its corresponding corrupted state $|\tilde{\psi}^\mu\rangle$, we find the quench layer number m^* such that the intermediate model distribution p_m^* resembles the corrupted pattern most. Then we time-evolve $|\tilde{\psi}^\mu\rangle$ with the series of learned unitaries $\hat{\mathcal{U}}_i$ starting from m^* to obtain the retrieved state $|\hat{\psi}^\mu\rangle$, from which we can then obtain the retrieved pattern $\hat{\xi}^\mu$. Top row: after learning a single pattern (digit ‘0’), a complete ‘0’ can be retrieved from a partially corrupted ‘0’. Bottom row: after learning multiple patterns (superposition of digit ‘0’ and ‘1’), complete ‘0’ or ‘1’ can be selectively retrieved from partially corrupted ‘0’ and ‘1’, respectively.

As shown in the top row of Fig.5, in the case of a single pattern (a digit ‘0’), the MBL hidden Born machine

is able to retrieve a complete pattern from a corrupted pattern (a partially corrupted digit ‘0’). As shown in the bottom row of Fig.5, in the case of multiple patterns (a superposition of ‘0’ and ‘1’), the MBL hidden Born machine is able to selectively retrieve complete patterns (‘0’ or ‘1’) based on the input corrupted pattern⁸².

B. Learning quantum dataset

We have demonstrated the power of MBL Born machine in learning classical data of the toy MNIST digit patterns, now we explore the ability of the MBL Born machine in learning data obtained from measurements of quantum states. While quantum state tomography is the standard method for state reconstruction, it becomes a daunting task as the system size increases. In this respect, quantum machine learning has shown great success in learning quantum states from limited amount of data^{63–69}. In this section, we use the hidden Born machine to learn data obtained from quantum many-body states prepared by Eqn.(7) subject to a single layer of quench, but with disorder strengths h_d different from the phases that the hidden Born machine is trained in.

In Fig.6, we demonstrate the learning ability of Born machine in the thermal and MBL phase. In Fig.6 left/right, we compare the measurement outcome sampled from the exact simulation q_{data} in MBL/thermal phase (denoted as ETH) (shown in purple), with those learned via hidden Born machine trained in MBL phase (shown in blue). In the insets we show the classical fidelity between the model distribution p and data distribution q , $F(p, q) = (\sum_i \sqrt{p_i q_i})^2$. We see that the hidden Born machine trained in MBL phase is able to capture the underlying probability distribution obtained from both the MBL and thermal phases with high fidelity (~ 0.98), while the hidden Born machine trained in thermal phase fails to learn either. Notice that in order to learn the quantum state, one needs to perform measurement in the informationally-complete basis as reported in Ref.⁶⁹.

C. Learning parity dataset

In the previous sections, we have discuss the role of localization and emergent memory in learning various datasets, however, the role played by interaction in the many-body localized phase remains unclear. To shed light into the role of interaction and its interplay with disorder, here, we investigate the power of MBL phase in learning parity dataset and compare it with both thermal and Anderson localized phase which can be obtained by setting $J_{zz} = 0$ in Eqn.(6). Here, we consider the even parity dataset, which is defined as set of bit-string (b_1, b_2, \dots, b_L) of length L with $b_i \in \{0, 1\}$, such that the parity function $\Pi(b_1, b_2, \dots, b_L) := \sum_{i=1}^N b_i \bmod 2$ is equal to 0. While this is a classical bitstring, it appears

as measurement outcome of particular quantum observables in certain basis such as measurement outcome of GHZ state in the x -basis.

Previous studies has indicate challenging learning on this dataset, in particular training the Born machine based on MPS with gradient descent optimization schemes has encountered failures⁷⁰, while quantum inspired optimization schemes such as density matrix learning has shown great success with the caveat in their scaling⁷¹. Here, we investigate the power of our hidden Born machine across various phases in learning the parity dataset. Our numerical results (Fig.7) demonstrates the interesting fact that both the MBL phase and Anderson localized phase show better performance compare to the thermal phase. The better learning performance in these two phases suggest that the emergence of integral of motion and memory plays an important role in learning. We further notice that the MBL phase has a better performance even though the Anderson localized phase is known to have better memory. In the latter the strong localization prevents the transport of information across the system, leading to a lesser learning power. While the value of fidelity around $F_{\text{MBL}} = 0.75$ is not too high, reflecting the hardness of learning the parity dataset, our MBL hidden Born machine still shows a better performance compare to MPS Born machine which was reported a fidelity of $F_{\text{MPS}} = 0.48$ ⁷⁰. Our numerical results indicate the importance of the presence of both disorder and interaction in the MBL hidden Born machine, and suggests that successive quenches defined by the learning cuts through a path in the Hilbert space that harnesses both local memory and interaction in order to arrive the target state.

VI. CONCLUSION AND OUTLOOK

In this work, we have introduced the hidden MBL Born machine as a powerful quantum inspired generative model. Although parameterized quantum circuit has become one of the focal point in the realm of quantum machine learning, their training scheme poses many challenges as one requires to search in an exponential Hilbert space, which resembles finding a needle in haystack¹⁰. While other variational algorithms such as QAOA offer a different scheme of finding solution in Hilbert space which is akin to adiabatic computing, here, by utilizing unique properties of MBL phase such as localization and memory, we develop a Born machine evolving under MBL dynamics such that by optimizing over values of disorder at each site we can reach a desired target state in the Hilbert space.

Despite the localized nature of the MBL phase, we show the expressibility of the MBL Born machine by mapping the 2D XXZ chain into 2D Ising model with proven expressibility advantage. Furthermore, we show that by including hidden units, we obtain expressive power advantage over the basic Born machine. We numerically

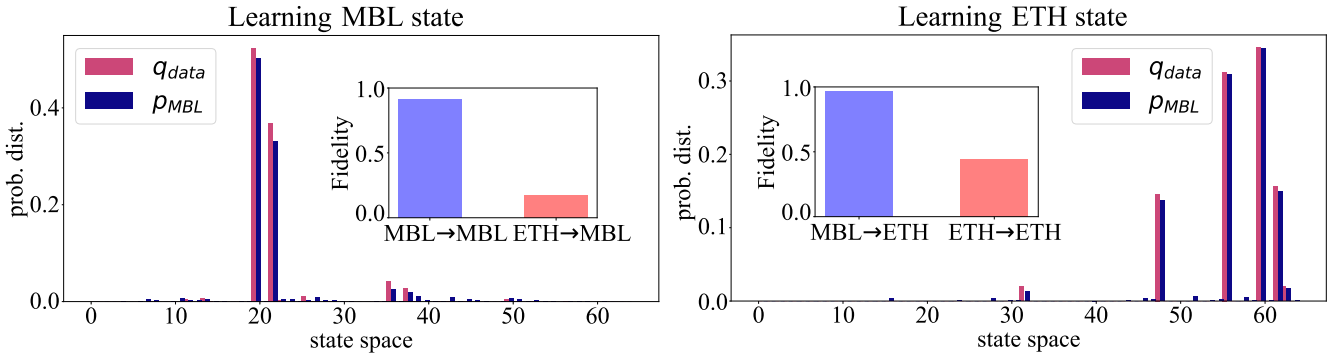


Figure 6: Learning quantum dataset. Left/right: MBL hidden Born machine trained in MBL phase learns the probability distribution corresponding to an MBL/thermal (denoted as ETH) target state. Insets: classical fidelities between the model and the data distributions. Model trained in the MBL phase has better learning capability than model trained in the thermal phase.

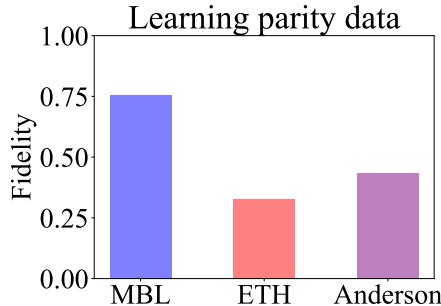


Figure 7: Learning parity dataset. Different bars in the horizontal-axis correspond to model trained in the MBL, thermal, and Anderson localized phases, respectively. Vertical-axis shows the classical fidelity of the model. Model trained in the MBL phase exhibits the highest fidelity despite the dataset is highly nonlocal. Comparing model performances in three phases suggest that both disorder and interaction are important for learning.

demonstrate this advantage in learning both classical and quantum data. In this work, we aimed to answer two key questions, namely, whether MBL phase can be used as resource for learning, and what is the underlying mechanism of learning. By performing various numerical experiments in the thermal phase, non-interacting Anderson localized phase, and the MBL phase, we show that successful learning relies on both interaction and localization during training.

Our work opens up a new horizon in utilizing exotic quantum phases of matter as quantum inspired generative models. While we have explored the role of disorder in the MBL phase, an immediate question that follows is whether other disordered quantum phase would be capable of learning, which is left for future work. Furthermore, our quenched Born machine resembles specific adiabatic schedule, and whether we can utilize our model as quantum variational algorithm awaits further investi-

gation. Although we have quantified the learning mechanism during the training by tracking both local and non-local quantities such as Hamming distance and entanglement entropy, more quantitative studies such as the existence of Barren Plateau and over-parametrization in the context of quantum kernel learning remains an important question for future study^{10,72,73}.

Acknowledgments

The authors would like to thank Nishad Maskara and Nicole Yunger Halpern for useful discussions. W.Z. acknowledges supports from IBM Research (Quantum) summer internship program. SFY would like to acknowledge funding from NSF (through CUA and Q-SeNSE) and AFOSR.

¹ P. Ball et al., *Nature* **599**, 542 (2021).

² F. Arute, K. Arya, R. Babbush, D. Bacon, J. C. Bardin, R. Barends, R. Biswas, S. Boixo, F. G. Brandao, D. A. Buell, et al., *Nature* **574**, 505 (2019).

³ E. Pednault, J. A. Gunnels, G. Nannicini, L. Horesh, and R. Wisnieff, arXiv preprint arXiv:1910.09534 (2019).

⁴ H.-S. Zhong, H. Wang, Y.-H. Deng, M.-C. Chen, L.-C. Peng, Y.-H. Luo, J. Qin, D. Wu, X. Ding, Y. Hu, et al., *Science* **370**, 1460 (2020), <https://www.science.org/doi/pdf/10.1126/science.abe8770>, URL <https://www.science.org/doi/abs/10.1126/science.abe8770>.

⁵ M. Gong, S. Wang, C. Zha, M.-C. Chen, H.-L. Huang, Y. Wu, Q. Zhu, Y. Zhao, S. Li, S. Guo, et al., *Science* **372**, 948 (2021), <https://www.science.org/doi/pdf/10.1126/science.abg7812>, URL <https://www.science.org/doi/abs/10.1126/science.abg7812>.

⁶ Y. Wu, W.-S. Bao, S. Cao, F. Chen, M.-C. Chen, X. Chen, T.-H. Chung, H. Deng, Y. Du, D. Fan, et al., *Physical review letters* **127**, 180501 (2021).

⁷ S. Ebadi, T. T. Wang, H. Levine, A. Keesling, G. Semeghini, A. Omran, D. Bluvstein, R. Samajdar, H. Pichler, W. W. Ho, et al., *Nature* **595**, 227 (2021).

⁸ J. R. McClean, J. Romero, R. Babbush, and A. Aspuru-Guzik, *New Journal of Physics* **18**, 023023 (2016).

⁹ E. Farhi, J. Goldstone, and S. Gutmann, arXiv preprint arXiv:1411.4028 (2014).

¹⁰ J. R. McClean, S. Boixo, V. N. Smelyanskiy, R. Babbush, and H. Neven, *Nature communications* **9**, 1 (2018).

¹¹ D. Marković and J. Grollier, *Applied Physics Letters* **117**, 150501 (2020).

¹² P. Pfeiffer, I. Egusquiza, M. Di Ventra, M. Sanz, and E. Solano, *Scientific reports* **6**, 1 (2016).

¹³ T. Gonzalez-Raya, X.-H. Cheng, I. L. Egusquiza, X. Chen, M. Sanz, and E. Solano, *Physical Review Applied* **12**, 014037 (2019).

¹⁴ T. Gonzalez-Raya, E. Solano, and M. Sanz, *Quantum* **4**, 224 (2020).

¹⁵ E. Torrontegui and J. J. García-Ripoll, *EPL (Europhysics Letters)* **125**, 30004 (2019).

¹⁶ K. Fujii and K. Nakajima, in *Reservoir Computing* (Springer, 2021), pp. 423–450.

¹⁷ K. Nakajima, K. Fujii, M. Negoro, K. Mitarai, and M. Kitagawa, *Physical Review Applied* **11**, 034021 (2019).

¹⁸ R. A. Bravo, K. Najafi, X. Gao, and S. F. Yelin, arXiv preprint arXiv:2111.10956 (2021).

¹⁹ W. Xia, J. Zou, X. Qiu, and X. Li, *Frontiers of Physics* **17**, 1 (2022).

²⁰ Z.-Y. Han, J. Wang, H. Fan, L. Wang, and P. Zhang, *Physical Review X* **8**, 031012 (2018).

²¹ S. Cheng, L. Wang, T. Xiang, and P. Zhang, *Phys. Rev. B* **99**, 155131 (2019), URL <https://link.aps.org/doi/10.1103/PhysRevB.99.155131>.

²² A. M. Gomez, S. F. Yelin, and K. Najafi, *Reconstructing quantum states using basis-enhanced born machines* (2022), URL <https://arxiv.org/abs/2206.01273>.

²³ H.-J. Liao, J.-G. Liu, L. Wang, and T. Xiang, *Phys. Rev. X* **9**, 031041 (2019), URL <https://link.aps.org/doi/10.1103/PhysRevX.9.031041>.

²⁴ D. A. Huse, R. Nandkishore, V. Oganesyan, A. Pal, and S. L. Sondhi, *Phys. Rev. B* **88**, 014206 (2013), URL <https://link.aps.org/doi/10.1103/PhysRevB.88.014206>.

²⁵ B. Altshuler, H. Krovi, and J. Roland, *Proceedings of the National Academy of Sciences* **107**, 12446 (2010).

²⁶ R. Martínez-Peña, G. L. Giorgi, J. Nokkala, M. C. Soriani, and R. Zambrini, *Physical Review Letters* **127** (2021), URL <https://doi.org/10.1103/PhysRevLett.127.100502>.

²⁷ J. Tangpanitanon, S. Thanasisl, N. Dangniam, M.-A. Lemonde, and D. G. Angelakis, *Physical Review Research* **2**, 043364 (2020).

²⁸ X. Gao, S.-T. Wang, and L.-M. Duan, *Physical Review Letters* **118** (2017), URL <https://doi.org/10.1103/PhysRevLett.118.040502>.

²⁹ J.-G. Liu and L. Wang, *Physical Review A* **98**, 062324 (2018).

³⁰ S. Cheng, J. Chen, and L. Wang, *Entropy* **20**, 583 (2018).

³¹ M. Benedetti, D. Garcia-Pintos, O. Perdomo, V. Leyton-Ortega, Y. Nam, and A. Perdomo-Ortiz, *npj Quantum Information* **5**, 1 (2019).

³² M. Benedetti, E. Lloyd, S. Sack, and M. Fiorentini, *Quantum Science and Technology* **4**, 043001 (2019).

³³ B. Coyle, D. Mills, V. Danos, and E. Kashefi, *npj Quantum Information* **6**, 1 (2020).

³⁴ P. Smolensky, Tech. Rep., Colorado Univ at Boulder Dept of Computer Science (1986).

³⁵ G. E. Hinton and R. R. Salakhutdinov, *science* **313**, 504 (2006).

³⁶ D. H. Ackley, G. E. Hinton, and T. J. Sejnowski, *Cognitive science* **9**, 147 (1985).

³⁷ P. Mehta, M. Bukov, C.-H. Wang, A. G. Day, C. Richardson, C. K. Fisher, and D. J. Schwab, *Physics reports* **810**, 1 (2019).

³⁸ X. Gao and L.-M. Duan, *Nature communications* **8**, 1 (2017).

³⁹ J. M. Deutsch, *Phys. Rev. A* **43**, 2046 (1991), URL <https://link.aps.org/doi/10.1103/PhysRevA.43.2046>.

⁴⁰ M. Srednicki, *Physical Review E* **50**, 888 (1994).

⁴¹ P. W. Anderson, *Phys. Rev.* **109**, 1492 (1958), URL <https://link.aps.org/doi/10.1103/PhysRev.109.1492>.

⁴² D. Basko, I. Aleiner, and B. Altshuler, *Annals of Physics* **321**, 1126 (2006), URL <https://doi.org/10.1016/j.aop.2005.11.014>.

⁴³ V. Oganesyan and D. A. Huse, *Phys. Rev. B* **75**, 155111 (2007), URL <https://link.aps.org/doi/10.1103/PhysRevB.75.155111>.

⁴⁴ J. Smith, A. Lee, P. Richerme, B. Neyenhuis, P. W. Hess, P. Hauke, M. Heyl, D. A. Huse, and C. Monroe, *Nat. Phys.* **12**, 907 (2016).

⁴⁵ D. J. Luitz, N. Laflorencie, and F. Alet, *Phys. Rev. B* **91**, 081103 (2015), URL <https://link.aps.org/doi/10.1103/PhysRevB.91.081103>.

⁴⁶ A. Pal and D. A. Huse, *Phys. Rev. B* **82**, 174411 (2010), URL <https://link.aps.org/doi/10.1103/PhysRevB.82.174411>.

⁴⁷ T. Devakul and R. R. P. Singh, *Phys. Rev. Lett.* **115**, 187201 (2015), URL <https://link.aps.org/doi/10.1103/PhysRevLett.115.187201>.

⁴⁸ L. Bottou et al., *Proceedings of Neuro-Nîmes* **91**, 12 (1991).

⁴⁹ I. Goodfellow, Y. Bengio, and A. Courville, *Deep learning*

(MIT press, 2016).

⁵⁰ L. Deng, IEEE Signal Processing Magazine **29**, 141 (2012).

⁵¹ P. Hauke and M. Heyl, Physical Review B **92** (2015), URL <https://doi.org/10.1103%2Fphysrevb.92.134204>.

⁵² J. H. Bardarson, F. Pollmann, and J. E. Moore, Phys. Rev. Lett. **109**, 017202 (2012), URL <https://link.aps.org/doi/10.1103/PhysRevLett.109.017202>.

⁵³ M. Serbyn, Z. Papić, and D. A. Abanin, Phys. Rev. B **90**, 174302 (2014), URL <https://link.aps.org/doi/10.1103/PhysRevB.90.174302>.

⁵⁴ D. A. Huse, R. Nandkishore, and V. Oganesyan, Physical Review B **90** (2014), URL <https://doi.org/10.1103%2Fphysrevb.90.174202>.

⁵⁵ E. Winfree, *Algorithmic self-assembly of DNA* (California Institute of Technology, 1998).

⁵⁶ L. Qian, D. Soloveichik, and E. Winfree, in *International Workshop on DNA-Based Computers* (Springer, 2010), pp. 123–140.

⁵⁷ A. Murugan, Z. Zeravcic, M. P. Brenner, and S. Leibler, Proceedings of the National Academy of Sciences **112**, 54 (2015).

⁵⁸ W. Zhong, D. J. Schwab, and A. Murugan, Journal of Statistical Physics **167**, 806 (2017).

⁵⁹ J. O'Brien and A. Murugan, ACS Synthetic Biology **8**, 826 (2019).

⁶⁰ M. Stern, M. B. Pinson, and A. Murugan, Physical Review X **10**, 031044 (2020).

⁶¹ W. Zhong, J. M. Gold, S. Marzen, J. L. England, and N. Yunger Halpern, Scientific reports **11**, 1 (2021).

⁶² M. Stern and A. Murugan, arXiv preprint arXiv:2206.05831 (2022).

⁶³ J. Carrasquilla, G. Torlai, R. G. Melko, and L. Aolita, Nature Machine Intelligence **1**, 155 (2019), ISSN 2522-5839, URL <http://www.nature.com/articles/s42256-019-0028-1>.

⁶⁴ G. Torlai, G. Mazzola, J. Carrasquilla, M. Troyer, R. Melko, and G. Carleo, Nature Physics **14**, 447 (2018).

⁶⁵ J. Wang, Z.-Y. Han, S.-B. Wang, Z. Li, L.-Z. Mu, H. Fan, and L. Wang, Physical Review A **101**, 032321 (2020).

⁶⁶ H.-Y. Huang, R. Kueng, G. Torlai, V. V. Albert, and J. Preskill, arXiv preprint arXiv:2106.12627 (2021).

⁶⁷ H.-Y. Huang, R. Kueng, and J. Preskill, Nature Physics **16**, 1050 (2020), ISSN 1745-2473, 1745-2481, URL <http://www.nature.com/articles/s41567-020-0932-7>.

⁶⁸ A. Elben, S. T. Flammia, H.-Y. Huang, R. Kueng, J. Preskill, B. Vermersch, and P. Zoller, *The randomized measurement toolbox* (2022), URL <https://arxiv.org/abs/2203.11374>.

⁶⁹ A. McClain Gomez, S. F. Yelin, and K. Najafi, arXiv e-prints pp. arXiv-2206 (2022).

⁷⁰ K. Najafi, M. E. Stoudenmire, S. Yelin, A. Azizi, X. Gao, M. D. Lukin, and M. Mohseni, in *34th Conference on Neural Information Processing Systems* (2020), First Workshop on Quantum Tensor Networks in Machine Learning, p. 10.

⁷¹ T.-D. Bradley, E. M. Stoudenmire, and J. Terilla, Machine Learning: Science and Technology **1**, 035008 (2020), URL <https://doi.org/10.1088%2F2632-2153%2Fab8731>.

⁷² T. L. Patti, K. Najafi, X. Gao, and S. F. Yelin, Phys. Rev. Research **3**, 033090 (2021), URL <https://link.aps.org/doi/10.1103/PhysRevResearch.3.033090>.

⁷³ J. Liu, K. Najafi, K. Sharma, F. Tacchino, L. Jiang, and A. Mezzacapo, arXiv preprint arXiv:2203.16711 (2022).

⁷⁴ J. J. Hopfield, Proceedings of the national academy of sciences **79**, 2554 (1982).

⁷⁵ P. Weinberg and M. Bukov, SciPost Physics **2**, 003 (2017).

⁷⁶ P. Weinberg and M. Bukov, SciPost Physics **7**, 020 (2019).

⁷⁷ R. Nandkishore and D. A. Huse, arXiv preprint arXiv:1404.0686 (2014).

⁷⁸ F. Alet and N. Laflorencie, Comptes Rendus Physique **19**, 498 (2018).

⁷⁹ D. A. Abanin, E. Altman, I. Bloch, and M. Serbyn, Reviews of Modern Physics **91** (2019), URL <https://doi.org/10.1103%2Frevmodphys.91.021001>.

⁸⁰ Note that for the proof in Ref.²⁸ to work, one also need to initialize the system in all $|+\rangle$ states and subsequently perform all measurements in the x -basis

⁸¹ While there exists other more sophisticated encoding schemes, here we choose the simplest one for illustration.

⁸² However, one should note that just like in classical pattern recognition⁷⁴, if the input pattern gets too corrupted and does not resemble any of the encoded patterns, this procedure will fail.

Appendix A: MBL phase transition

In this section, we present the details of the numerical simulation of XXZ model (Eqn.(6)) and confirm the thermal to MBL phase transition. We simulate the XXZ model using exact diagonalization methods provided by the QuSpin package^{75,76}. Throughout the paper we use parameters $J_{xy} = J_{zz} = 1$.

One hallmark of the MBL phase is the Poisson distribution of level spacings in the eigenspectrum of the Hamiltonian.^{77–79} The level statistics $Pr(r_\alpha)$ is defined as the normalized distribution of

$$r_\alpha = \frac{\min(\Delta_{\alpha+1}, \Delta_\alpha)}{\max(\Delta_{\alpha+1}, \Delta_\alpha)}, \quad (\text{A1})$$

where $\Delta_\alpha = E_{\alpha+1} - E_\alpha$ are the level spacings in the eigenspectrum. In Fig.8, we show the level statistics in a simulation of $L = 16$ spins described by Eqn.(7) subject to a single quench $M = 1$, at two different disorder strengths: $h_d = 0.1$ and $h_d = 3.9$ (the critical disorder strength is $h_c \sim 3.5$ for $J_{zz} = J_{xy} = 1$). We see that indeed the level statistics in the thermal phase obeys Wigner-Dyson statistics, and in the MBL phase obeys Poisson statistics, confirming the existence of thermal-MBL phase transition.

Another hallmark of MBL phase is the area law scaling of von Neumann entanglement entropy ($S_{\text{ent}} = -\text{Tr}\rho \ln \rho$), compared to the volume law scaling in the thermal phase. We numerically calculate the half-system entanglement entropy in the middle of the spectrum for the Hamiltonian in Eqn.(7), and perform a scaling analysis for different L and different disorder strengths h (see Fig.9). Our numerical results agrees with those reported in⁴⁵.

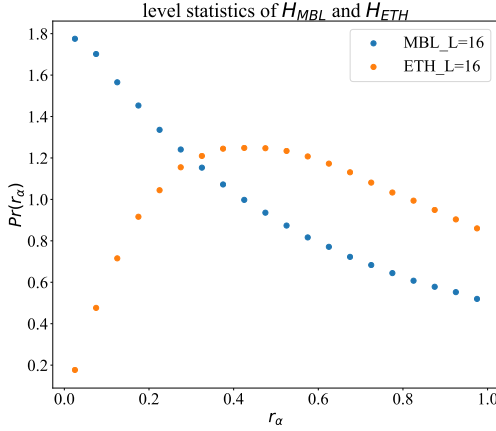


Figure 8: Level statistics of $L = 16$ XXZ model subject to quenches in the z -direction. The thermal phase (denoted as ETH) is simulated with $h_d = 0.1$ and the MBL phase is simulated with $h_d = 3.9$. Results are averaged over 1000 different realizations.

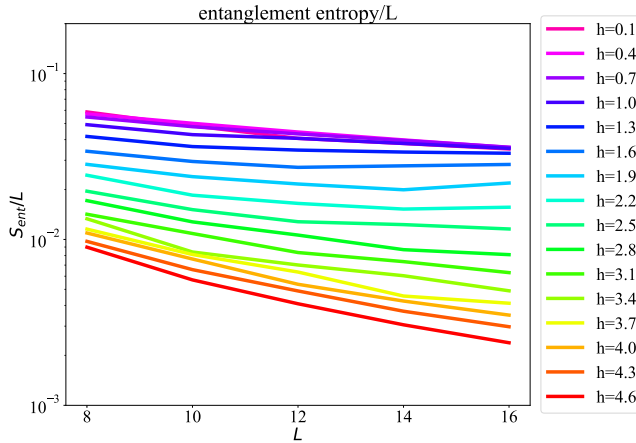


Figure 9: Scaling analysis of entanglement entropy. We plot the entanglement entropy per site S_{ent}/L as a function of system size L for different disorder strengths h . Volume law scaling in the thermal phase (small h) leads to constant S_{ent}/L , while area law scaling in the MBL phase (for large h) leads to decreasing S_{ent}/L .

Appendix B: Training MBL hidden Born machine

Previously, KL-divergence has been suggested for training MBL Born machine as a generative model²⁷. However, KL-divergence does not capture correlations within data, and suffers from infinities outside the support of data distribution. To remedy these situations, the Maximum Mean Discrepancy (MMD) loss has been proposed for training Born machines²⁹. The MMD loss measures the distance between model distribution p and target distribution q , by comparing their mean embeddings in the feature space. The (squared) MMD loss can

be written as

$$\begin{aligned} \mathcal{L}_{MMD} &= \left\| \sum_x p(x) \phi(x) - \sum_x q(x) \phi(x) \right\|^2 \\ &= \mathbb{E}_{x, x' \sim p} k(x, x') + \mathbb{E}_{y, y' \sim q} k(y, y') \\ &\quad - 2 \mathbb{E}_{x \sim p, y \sim q} k(x, y), \end{aligned} \quad (\text{B1})$$

where we have employed the kernel trick and write $k(x, y) = \phi(x)^T \phi(y)$. In our model, we use a Gaussian mixture kernel $k(x, y) = \frac{1}{c} \sum_{i=1}^c \exp\left(-\frac{1}{2\sigma_i^2} |x - y|^2\right)$ of four channels $c = 4$, with corresponding bandwidths $\sigma_i^2 = [0.1, 0.25, 4, 10]$. The bandwidths are chosen such that our Gaussian kernels are able to capture both the local features and the global features in the target distribution.

In the training of our MBL hidden Born machine, we use $N = 6 + 2$ (6 visible spins and 2 hidden spins), and $M = 100$ quenches and search over $N = 500$ different disorder realizations.

Appendix C: Data encoding

Here, we describe the detailed data encoding scheme and our toy dataset of MNIST digit patterns in this section. Given a reduced density matrix ρ_{vis} of L visible spins, we compute the distribution of finding each of the 2^L basis states in our computational basis, and interpret the result as pixel values. We then reshape this probability vector into an image of size $2^{L/2} \times 2^{L/2}$.

On the other hand, given an image $\vec{x}_\mu \in \mathbb{R}^{n \times n}$, where $n \times n$ is the number of original pixels in the image, we first downsample it to $2^{L/2} \times 2^{L/2}$ pixels, then normalized the pixel values to be within 0 and 1.

Our toy dataset of MNIST digit patterns are constructed as follows: we take all the training images \vec{x}^μ from a digit class, downsample to $2^{L/2} \times 2^{L/2}$ pixels, and compute each pixel as the average value $\bar{x}_i = 1/P \sum_{\mu=1}^P x_i^\mu$ across different styles within this digit class, where $i = 1, \dots, 2^L$. We then normalized the pixels to $\bar{x}_i \rightarrow \bar{x}_i / \sum_i \bar{x}_i$ and interpret the result as q_{data} . We take caution that this is different from learning the MNIST distribution in generative models. The latter refers to learning the joint probability distribution over all pixels in the image, and our toy data set corresponds to taking the mean-field limit of this joint probability distribution, which ignores the complicated correlations among pixels. This is akin to learning a single pattern (the averaged MNIST images shown in Fig.2), and the reason for taking the average pixel value is such that we will be able to perform pattern recognition with imperfect initial states.